Oral presentation | Multi-phase flow
Multi-phase flow-IV
Tue. Jul 16, 2024 10:45 AM - 12:45 PM Room D

[4-D-01] Numerical modeling of wave impact on a vertical wall with a deflector

Sergio Croquer Perez[1], *Sébastien Poncet[1], R.W. Jay Lacey[1] (1. Université de Sherbrooke)

Keywords: Wave impact, RANS modeling, Vertical wall, Volume Of Fluid, Overflow rate

Twelfth International Conference on
Computational Fluid Dynamics (ICCFD12),
Kobe, Japan, July 14-19, 2024

Numerical modeling of wave impact on a vertical wall with a deflector

S. Croquer Perez, S. Poncet and R.W.J. Lacey
Corresponding author: Sebastien.Poncet@USherbrooke.ca
Université de Sherbrooke, Canada.

Abstract: Infrastructures located on the seashore are protected by coastal structures like vertical walls or breakwaters. Due to sea level rise, there is an urgent need to develop new design rules for these structures adapted to local wave conditions and bathymetry. In that context, the present work proposes an extensive numerical analysis of 20 wave conditions for three still water levels and three vertical walls equipped or not with a curved deflector. The wave characteristics and bathymetry correspond to conditions measured in the gulf of the Saint-Lawrence river (Québec, Canada). The main result is that the 60° deflector can reduce overtopping by up to 95% for large relative elevations, while the 30° deflector has no effect or can even deteriorate overtopping compared to the plane vertical wall under some conditions. The results demonstrate also that the common correlation widely considered in the literature fail to predict this behavior, highlighting the necessity to develop high-fidelity numerical solver for such complex flows.

Keywords: Wave impact, Overtopping, Vertical protective wall, Curved parapet, Computational Fluid Dynamics.

1 Introduction

About 40% of the world population lives directly on the seashore. These regions are progressively affected by the sea level rise, as a consequence of global climate change. This situation requires an urgent and proper quantification of the performance of protective coastal structures before proposing mitigation alternatives. The most commonly built coastal protection structures include breakwaters and vertical walls. The latters are usually built to protect against violent wave impacts in coastal areas close to beaches and with intense human activity. The main two possible consequences of these violent wave events on coastal structures are (i) erosion and progressive destruction of the structures and (ii) overtopping, which can induce flooding of the coastal roads. To prevent overflow, some modifications to protective structures have been progressively proposed: addition of parapets/deflectors at the top of the wall [1], construction of submerged walls before the dike [2], and substitution of the vertical wall with curved geometries (recurves) [3].

Predicting the forces applied by the waves on structures and the associated overtopping is of prime importance to better design the protective structures. All methods are based on both the wall geometry (with or without deflector) and the wave characteristics, usually defined for deep water conditions, such that they are not affected by the bathymetry [4]. However, the wave type approaching the wall and the associated impact depend on many other parameters: length of the berm, still water level (SWL), incident wave height . . . [5]. For impacts on breakwaters, McConnell [6] proposed four possible scenarii: pulsating or quasi-static waves, weakly breaking waves, breaking waves and bursting waves. For a vertical wall, the induced forces depend strongly on the incident waves. Cuomo et *al*. [7] categorized them into two classes: pulsating or quasi-static forces and impact forces. These last forces act on the structure during a time period comparable to the natural vibration period of the structure and are associated with breaking impacts. Pulsating forces are associated with quasi-static and breaking waves.

Methods used to determine the forces on protective structures are generally empirical. As shown by Castellino et *al*. [8], these methods used to predict the horizontal and uplift forces on dams remain applicable to vertical walls. For quasi-static forces, one could cite the methods of Sainflou [9] for stationary waves or Goda [10], which accounts for the berm's effect, the buoyancy of the box . . . . This last method still remains the most used one for quasi-static forces. For breaking waves, a huge variety of correlations exist but none of them provides satisfactory results for all conditions due to the stochastic character of the impacts. Moreover, some methods like the one proposed by Bagnold [11] require to know the sizes of the trapped air pockets, which is difficult to determine for realistic structures.

For overtopping, two main regimes are usually observed. When waves break at the top of the wall or behind it, overtopping is characterized by a continuous water flow and is known as green-water overtopping. For breaking waves on the wall surface or just before, the spray of droplets can surpass the wall due to wind effects but it generally

does not generate huge overtopping volumes [12]. Deflectors or parapets are used to reduce this overtopping by deflecting the wave seawards without considerably increasing the seawall height. The positive effect of deflectors and parapets has been illustrated for various coastal structures. According to [1], it depends on freeboard (R_c) to significant wave height (H_s) ratio. Overtopping becomes negligible for $R_c/H_s \geq 1.5$ (resp. ≥ 1.05) for plane (resp. curved) deflectors. On the contrary, for $R_c/H_s \leq 1.2$, the positive effect vanishes. Overtopping is usually quantified using the overtopping rate q defined as the volume of water surpassing the wall during a given period of time. q can be generally approximated by an exponential function, which includes R_c and H_s, among other parameters.

Even if empirical correlations and analytical models remain valuable tools to have an approximate design of protective structures, their applicability and accuracy remain limited and they often include parameters, which are difficult to determine. Thus, small or large scale experiments are still deemed necessary to validate or refine these models or to develop more accurate ones. Recently, Stagonas et $al.$ [13] performed experimental measurements of wave loads acting on a seawall equipped with three different recurves for regular waves. For the same incoming wave conditions, the shape of the recurve was varied by increasing the length of its arc. They showed that the deflected water flow does not alter the next upcoming wave. Also, for purely pulsating conditions, the influence of the arc length on (mean) peak pressures and forces was found to be negligible. On the contrary, increasing the arc length leads to an increase of the mean of the maximum impulsive pressure and force peaks. Croquer et $al.$ [14] performed a statistical basis using experimental data from INRS to determine the most influencing parameters on forces and overtopping over vertical walls. Horizontal force and overtopping data were measured for regular waves of varying height (0.63–1.65 m), period (4–8 s), and water depth (3.37–3.97 m) over a vertical wall. The redundancy analysis showed that about 60% of the output variable variance can be explained by the structure dimensions and 15% by the incoming wave characteristics. The minimum errors for the average force and overtopping remained quite high, at 39.9% and 22.1%, respectively, demonstrating the difficulty of statistical models to predict such complex behaviors.

In this context, numerical models based on turbulence closure represent valuable tools to quantify interactions between extreme waves and coastal structures. One could cite the work of González-Cao et $al.$ [15], who compared the performances of two solvers, DualSPHysics and IHFOAM, to reproduce the propagation of a regular wave train and its collision with a vertical sea wall with a horizontal cantilever slab. The main result was that the mesh-less model named DualSPHysics provided acceptable results compared to the experiments and IHFOAM. More recently, Croquer et $al.$ [16] developed a two-phase Favre-Averaged Navier–Stokes (FANS) model based on OpenFOAM libraries to study wave dynamic interactions with impermeable structures. The model took into account air compressibility as well as turbulence effects through the $k-\omega$ SST closure. After a careful validation on two testcases, the model was used for the analysis of wave interactions with vertical walls (without deflector) along the Saint-Lawrence Bay (Quebec) in Canada. Four incident wave cases representing frequent and extreme storm conditions were considered and the results discussed in terms of hydrodynamic loads and overtopping for two breaking and two non-breaking wave cases. Castellino [17] investigated confined-crest impact on a vertical wall equipped with a recurved deflector. While the geometry of the deflector remained fixed, the author quantified the influence of the toe berm's geometry on the impulsive forces obtained on the wall. The numerical predictions using the OpenFOAM libraries were fist compared to Goda's model in terms of pressure distribution to validate the model. The k$-\varepsilon$ closure was preferred over the k-ω SST model. She demonstrated that the intensity of the confined-crest impacts increases by increasing the berm's height because of shoaling effect.

This brief literature review demonstrates the lack of reliable numerical data from a well-validated model for the forces and overtopping over a vertical wall equipped with a curved deflector and for a wide range of realistic wave conditions. The objective of the present work is then to extend the former work of Croquer et $al.$ [16] and to investigate the wave interactions with vertical walls equipped or not with a curved deflector, using the same model. Frequent and extreme events against a seawall located in the Saint-Lawrence Bay (Canada) are simulated accordingly for 20 wave conditions, 3 water depths and 3 geometries of the protective wall.

2 Numerical modeling

2.1 Geometrical modeling and operating conditions

The calculation domain and the offshore wave conditions correspond to the bathymetry and the measurements from a buoy located in the Saint-Lawrence river, in the North of the Gaspé peninsula ($49^o54'N\ 65^o76'W$) [18]. The 2D domain (1 : 46 scale) displayed in Figure 1a is 30 m height, and around 246 m long whose 86 m at the back of the vertical wall. The wall (6.5 m height) is located at the top of a beach with a 6% slope. The still water level (SWL), also named the water depth h, varies between 13.42 and 15.42 m from the bed or between 2.8 and 4.8 m from the wall's foot. The wall is equipped or not by a deflector whose angle is either 30 or 60°. Their dimensions

are given in Figures 1 c and d. Whatever the deflector, the total elevation of the wall remains at 17.12 m.

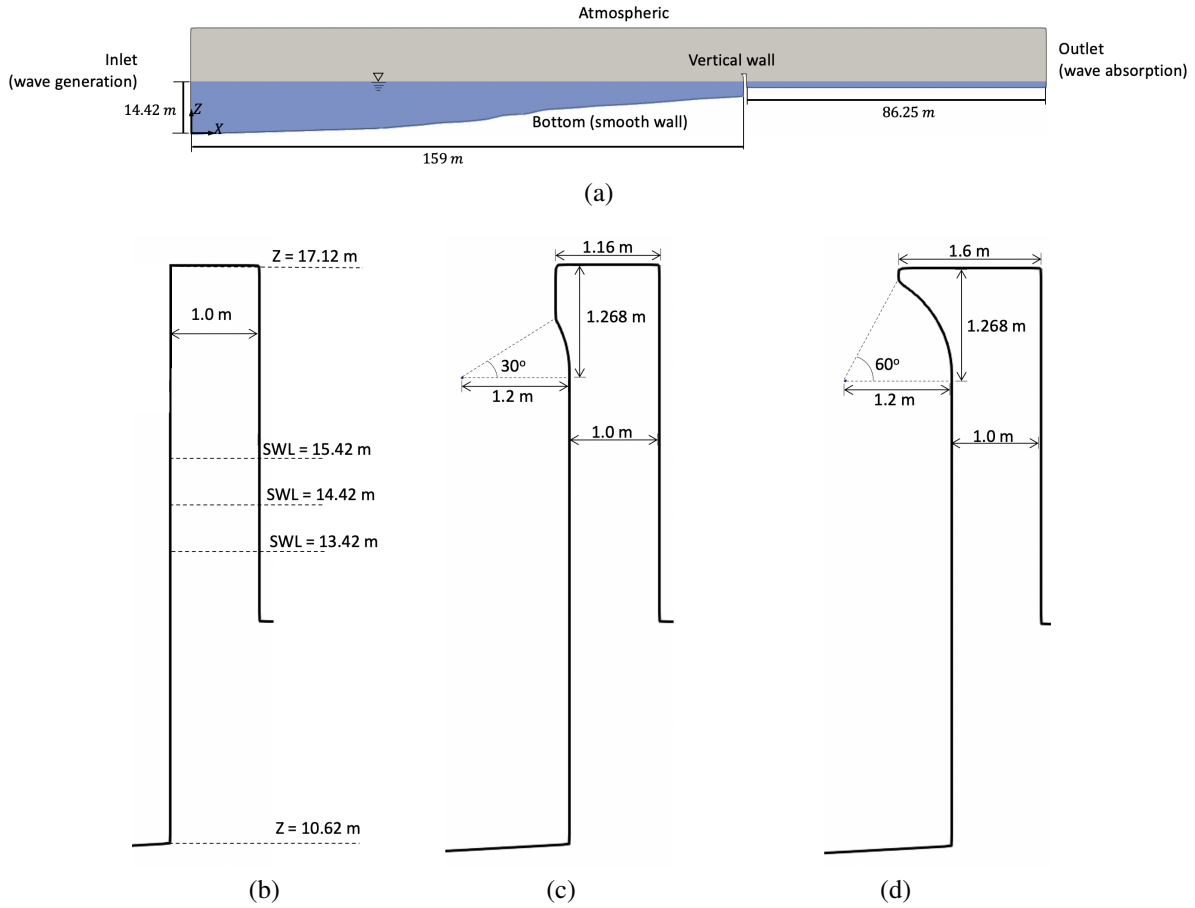

Figure 1: Computational domain of the vertical wall in the Saint-Lawrence Bay with the relevant boundary conditions. (a) Boundary conditions and dimensions for (b) the straight wall, (c) the wall with a 30° deflector and (d) the wall with a 60° deflector.

20 conditions of regular waves are first modeled using the Stokes II or V theories depending on their offshore height. They are generated by the *olaFlow* library at $X = 0$. The bed is supposed to be a no-slip wall. The upper limit of the domain is opened to the atmosphere, such that water is free to cross that boundary. The total pressure is fixed to $p_o = 101325$ Pa on it. The right limit of the domain is considered as an outlet with a zero velocity gradient condition able to absorb incident waves. The cases providing the highest force on the wall are repeated for the other values of SWL. The conditions are summarized in Figure 2, with $\frac{H_S}{L}$ the wave's slope and $\frac{h}{L}$ the relative depth. Note that H_S and L represent the significant wave height and the wave length, respectively.

2.2 Governing equations

The fluid is considered as a Newtonian pseudo-mixture of air (gas) and water (liquid), separated by a clear interface. Air and water share the same velocity and pressure fields. Bredmose et *al*. [19] showed that air pressure and density variations play a central role during certain wave impacts. Thus, air is assumed to be compressible and behaves as an adiabatic gas. The unsteady and turbulent flow field is modelled using the FANS equations:

$$\frac{\partial \rho}{\partial t} + \nabla \cdot (\rho \boldsymbol{u}) = 0 \tag{1}$$

$$\frac{\partial}{\partial t}(\rho \boldsymbol{u}) + \nabla \cdot (\boldsymbol{u} \rho \boldsymbol{u}) = -\nabla p^* + \nabla \cdot \left(\mu_{eff} \nabla \boldsymbol{u}\right) + \sigma \kappa \nabla \alpha - \boldsymbol{g} \boldsymbol{x} \nabla \rho \tag{2}$$

where ρ and $\boldsymbol{u} = u\hat{i} + v\hat{j} + w\hat{k}$ are, respectively, the mean flow density and velocity vector, α is the water volume fraction, $p* = p - \rho \boldsymbol{g} \boldsymbol{x}$ is the dynamic pressure, $\boldsymbol{g} = -9.81\hat{k}$ m s^{-2} is the gravity vector, $\boldsymbol{x}$ is the local position vector, μ_{eff} the effective dynamic viscosity, $\sigma = 0.07$ N m^{-1} the surface tension and $\kappa = \nabla \cdot \frac{\nabla \alpha}{|\nabla \alpha|}$ the interface curvature.

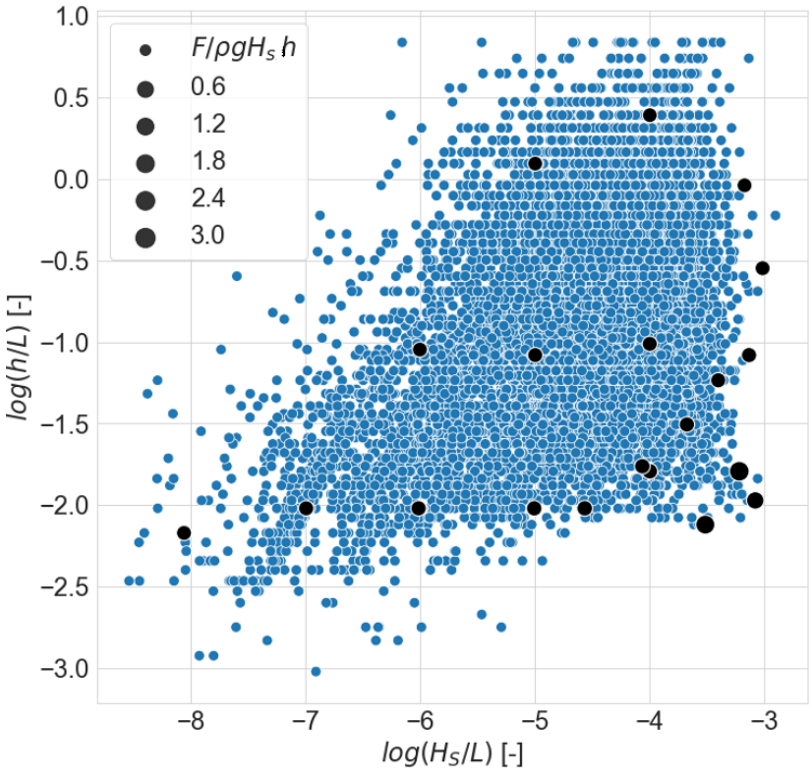

Figure 2: Wave conditions considered numerically (black) and data from a buoy (blue) with the force intensity F on the vertical wall.

2.2.1 Flow properties

The mean flow density (ρ) and effective viscosity (μ_{eff}) are determined using mixing-type laws:

$$\rho = \alpha\rho_w + (1-\alpha)\,\rho_a, \tag{3}$$

$$\mu_{eff} = \alpha\mu_w + (1-\alpha)\,\mu_a + \rho\nu_t \tag{4}$$

where ν_t is the turbulent kinematic viscosity. The subscripts a and w refer, respectively, to the air and water phases. In this study, ν_t, is calculated using the $k-\omega$ SST model [20].

Water density (ρ_w) is determined using a linear equation of state:

$$\rho_w = \rho_{0,w} + \Psi\,(p - p_0) \tag{5}$$

where p_0 =101.325 kPa, $\rho_{0,w}$=998 kg m^{-3} and $\Psi = (R_w T)^{-1}$ is the water compressibility factor (R_w = 3kJ kg^{-1} K^{-1}). Air density is computed using the adiabatic gas model:

$$\frac{p}{\rho_a^\gamma} = \frac{p_{ref}}{\rho_{ref}^\gamma} = const. \tag{6}$$

where $\gamma = 1.4$ is the air specific heat ratio and p_{ref} =1×10^5 Pa and ρ_{ref} =1 kg m^{-3} are, respectively, the reference pressure and density. This model neglects heat transfer effects, which allows the energy and momentum equations to be decoupled. The model can be used in the context of wave impact dynamics since the events occur within a very short time frame and both phases tend to have the same temperature [21].

2.2.2 Turbulence model

Turbulence effects are taken into account by using the compressible formulation of the $k-\omega$ SST turbulence model [20]. It computes the eddy viscosity (ν_t) by blending the $k-\omega$ model in the near wall region with the $k-\epsilon$ model in the free turbulence region. This approach is often preferred since it offers a good compromise in terms of accuracy versus complexity, specially when dealing with complex flow features. Specifically in wave dynamic

simulations, this approach shows better prediction of the turbulence levels around the interface when compared with other two-equation turbulence models [22].

2.2.3 Interface capture

The presented model assumes that air and water are separated by a distinct interface. The proper capture of the interface evolution throughout the simulation is important, as it describes the wave movement and influences the mean flow properties. The location of each phase within the domain is determined using the Volume of Fluid method [23], which defines the water volume fraction α such that $\alpha = 1$ in fully submerged cells and $\alpha = 0$ in dry cells. The interface is limited to a short distance (~ 2 mesh cells) where $0 < \alpha < 1$.

The α field at each time step is computed using the Multidimensional Universal Limiter with Explicit Solution (MULES) algorithm which introduces the following modified transport equation:

$$\frac{\partial \alpha}{\partial t} + \boldsymbol{u} \cdot \nabla \alpha + \nabla \cdot \boldsymbol{U_c} \alpha \left(1 - \alpha\right) = 0 \tag{7}$$

where $|\boldsymbol{U_c}| = min\left[c_\alpha |\boldsymbol{u}|, max\left(\boldsymbol{u}\right)\right]$ and c_α is an interface compression parameter. The main advantage of this approach is its numerical stability as it bounds $0 \geq \alpha \geq 1$. Nonetheless, it might be sensible to the grid orientation and requires a balanced scheme setup [24].

2.2.4 Wave generation modeling

The *olaFlow* library [25] was used for wave generation. This library includes a series of wave-generation boundary conditions which introduce the corresponding incoming interface elevation and associated velocity profiles at the domain boundary according to known wave theories (linear, Stokes II, Stokes V, Cnoidal, stream function and solitary wave). It also provides wave-absorption functions for inlet and outlet boundaries, which prevent non-physical reflections back into the domain. By implementing the functions along the domain boundaries, the *olaFlow* avoids the use of sponge-zones, thus avoiding enlarging the computational domain. Implementation details can be found in [26].

2.3 Numerical method

The model is implemented in OpenFOAM *v2006* by modifying the *compressibleInterNotFoam* solver. The modified version, deemed *compressibleInterNoTFoam*, drops the energy equation from the system, which simplifies convergence and reduces the computational costs. The adiabatic gas model is set up by typing in the corresponding Equation of State option (`adiabaticPerfectFluid`) within the file `/constant/thermoPhysicalProperties.air`. Both the adiabatic gas model and the MULES algorithm were chosen via a numerical benchmark study where this combination performed better than other setups using the perfect gas model and/or the isoAdvector algorithm [27]. The finite volume method is used to discretize and solve the resulting system of equations. Table 1 lists the numerical parameters. Advection and diffusion terms are discretized using, respectively, upwind and central second-order schemes. The first-order Euler temporal scheme is employed for the temporal terms. Second-order and Crank-Nicholson temporal schemes were tried out in preliminary calculations but proved to be unstable or required excessively small time steps (10^{-12} s) without any noticeable improvement on the results. The pressure-velocity coupling is resolved via the PIMPLE algorithm, *i.e.* a merge between the Pressure-Implicit with Splitting Operators (PISO) and the Semi-Implicit Method for Pressure Linked Equations (SIMPLE) algorithms, with improved accuracy for transient simulations [28].

Table 1: Summary of the fixed numerical parameters for all the configurations.

Parameter	**Definition**
Fluids	water-air
Water properties	liquid
Air properties	adiabatic gas
Turbulence model	$k - \omega$ SST
State	Transient
Temporal schemes	Euler (1^{st} order)
Diffusion scheme	Gauss linear (2^{nd} order)
Advection scheme	limitedLinear (2^{nd} order)
Solution algorithm	*PIMPLE*

2.4 Numerical parameters

The time step varies at each temporal iteration to respect a CFL number lower than 0.1. Each case was simulated over a 400 s time period, representing 40 waves per case in average. The structured mesh grid was generated using snappyHexMesh. Elements outside the domain are discarded and those along the boundaries are snapped to the geometry. The final mesh contains $1,180,019$ rectangular elements. The nominal element size is 0.05 m. This value was imposed from the inlet up to the wall. Element size was reduced by 2 to 4 times in the near bottom region and doubled behind the wall and away from the interest region. It proved to lead to grid-independent results. All cases were run on the Digital Research Alliance of Canada clusters *Cedar* (WestGrid) and *Niagara* (SciNet [29]), using 3 nodes having each 40 CPUs *Intel SkyLake* (2.4 GHz) and 202 Gb of RAM memory. The average calculation time for simulating 400 s of physical time is around 4 days.

It is noteworthy that the present model has already been carefully validated in [27] against two reference experimental test cases in 2D corresponding to: (i) a sloshing tank ; (ii) regular wave impacts against a vertical impermeable wall with a cantilever slab. The results were favorably compared to the experimental and numerical data of González-Cao et *al*. [15] for a 22.5 m long water flume (1.2 m wide and 1 m deep) and fixed wave conditions (height $H = 0.065$ m and period $T = 2.2$ s) in terms of water surface level and horizontal force on the wall.

3 Results and discussion

3.1 General topology of breaking impacts and the rule of the parapet

The main effect of the deflector during breaking impacts is presented on Figure 3 for a water depth at $X = 0$ equal to $h = 14.42$ m. This case corresponds to a significant wave height $H_S = 4.756$ m (at $X = 0$), an offshore wave height $H = 7.6$ m, and wave period and wave length equal to $T = 9.8$ s and $L = 103.6$ m, respectively. Whatever the wall geometry, the breaking impact is clearly visible with air pockets trapped in front of the structure and a strong vertical jet. For the base case without deflector, this jet is purely vertical and does not generate any significant overtopping. The deflector with a 30° angle (Fig.3b) has a horizontal projection of 0.16 m, such that it does not prevent from vertical jets. More importantly, the jet flow is pushed seawards by the parapet exhibiting a curved trajectory. The main consequence is that part of the jet falls back due to gravity behind the wall creating more overtopping compared to the plane wall case. It will be shown later that its influence remains most of the time negligible compared to the base case with no deflector (Fig.3a) but can get even negative for extreme events. The deflector with a 60° angle (Fig.3c) has a horizontal projection of 0.6 m, which deviates more the vertical jet. The jet reaches a lower height and is more curved, generating less overtopping compared to the 30° angle case. Yet, for specific conditions and both deflector geometries, the deviated jet and the incident wave peak can meet in front of the seawall, generating overtopping.

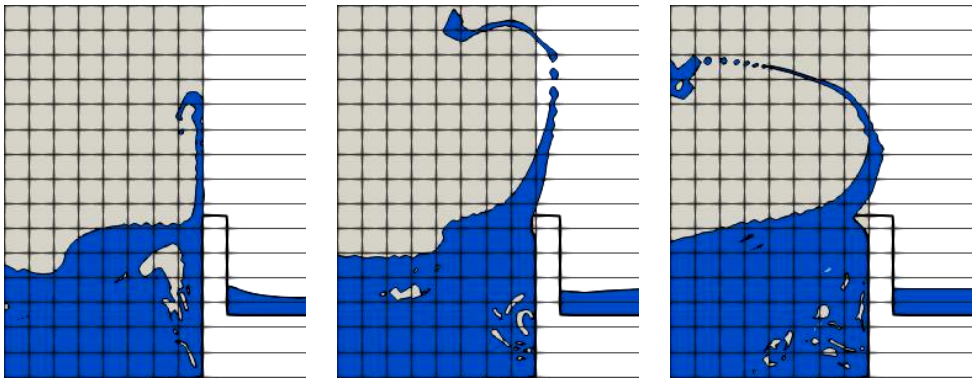

(a) (b) (c)

Figure 3: Examples of wave breakings for (a) a vertical wall, (b) a 30° deflector and (c) a 60° deflector. The wave period, length and significant height are $T = 9.8$ s, $L = 103.6$ m and $H_S = 4.756$ m, respectively. Results obtained for $h = 14.42$ m.

3.2 Influences of the deflector and the water depth for extreme wave conditions

It is noteworthy that, for all the 20 wave conditions, the maximum force has been obtained for the wave conditions: $T = 8.5$ s, $L = 86.6$ m, $H_S = 3.461$ m (and the 60° deflector). This case is then analysed here into more details.

Figure 4 presents first the temporal evolution of the horizontal force applied on the wall for the 60° deflector and three water depths. The maximum force increases from 500 kN/m for h = 13.42 to around 25 MN/m for h = 15.42 m. As the mean force profiles (black lines) do not exhibit oscillations, impacts can be considered as breaking impacts with small trapped air volumes.

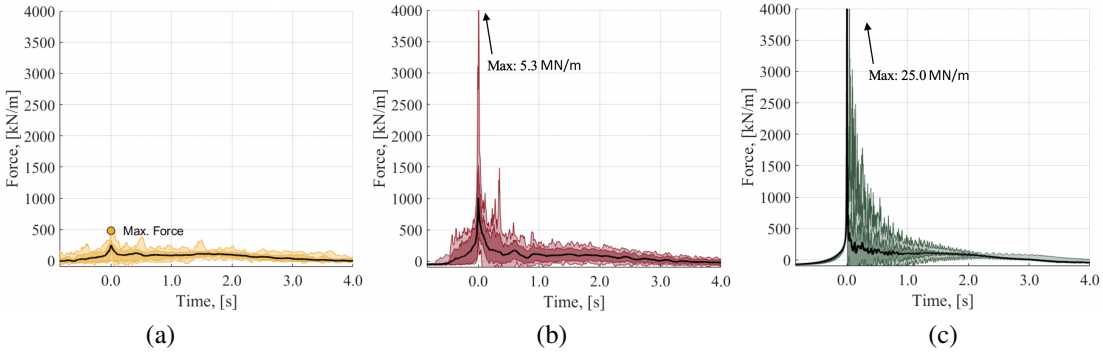

Figure 4: Temporal evolution of the horizontal force applied on the wall for the 60° deflector. Results obtained for the wave conditions (T = 8.5 s, L = 86.6 m, H_S = 3.461 m) and three water depths, (a) h = 13.42, (b) 14.42 and (c) 15.42 m.

Figure 5 displays the corresponding pressure contours on the wall for the same wave conditions, the 60° deflector and the same three water depths. In general, pressure is maximum close to the still water level. For h = 13.42 m (Fig.5a), the impact exhibits a lot of oscillations whose magnitude is similar to those associated with the initial impact. The maximum pressure is then 248.8 kPa. For h = 14.42 m (Fig.5b), the maximum pressure gets 710.1 kPa and oscillations are more pronounced and last til 4 s. For h = 15.42 m (Fig.5c), not surprisingly, the maximum pressure increases and reaches 9546.7 kPa but oscillations are rapidly dissipated and disappear before 1 s.

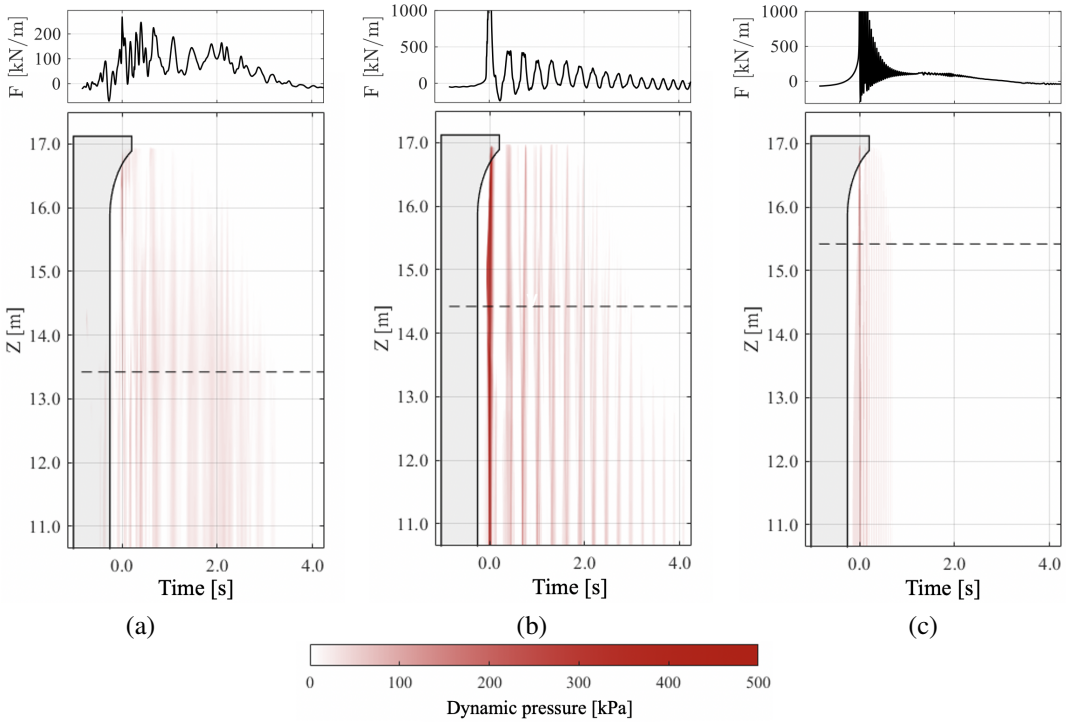

Figure 5: Temporal evolution of the dynamic pressure field in front of the wall. Same conditions as Figure 4.

For each impact, Cuomo et *al*. [7] distinguish two components: (i) the quasi-static load associated to the wave flowing along the wall and (ii) the impulsive load associated to the initial force peak. The impulsive component gets important for ram or breaking types impacts. Though maximal forces may vary a lot for similar conditions, Bullock et *al*. [30] showed that their impulsion Imp and rising time t_{rs} are uniform, appearing as valuable parameters

for the design of protective walls. These two parameters are defined in Figure 6. The rising time t_{rs} represents the time interval between $F = 0$ kN/m and $F = F_{max}$. The impulsion Imp can be simply estimated using the approximate relation provided by Chen et *al*. [31]: $Imp = t_{rs} F_{max}$.

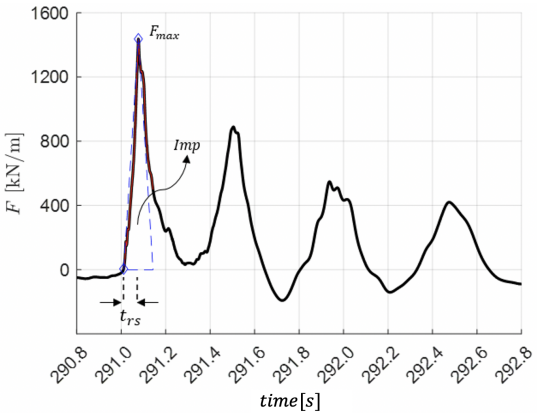

Figure 6: Definitions of the rising time (t_{rs}) and impulsion (Imp).

Table 2 summarizes the results in terms of maximum force, impulsion, average rising time and overflowrate for the wave conditions ($T = 8.5$ s, $L = 86.6$ m, $H_S = 3.461$ m) and three water depths, namely $h = 13.42$, 14.42 and 15.42 m. The maximum force varies with the water depth from 912 kN/m to 12.6 MN/m for h increasing from 13.42 to 15.42 m in the case of the vertical wall and the same trend is observed for both deflectors. In the same way, adding a deflector and increasing its angle favors higher maximum forces, though the wall geometry (deflector or not) does not change the type of impact for these wave conditions. A peculiar behavior is obtained for $h = 13.42$ m. At this water depth, F_{max} is lower with a parapet and decreases with the deflector angle. For a fixed water depth, the average rising time t_{rs} remains almost constant for the three geometries. As a consequence, the impulsion Imp follows the same trends as the maximum force F_{max}. The only exception is obtained for $h = 13.42$ m, where the rising time seems particularly long for the 60° deflector. So Imp increases by increasing the water depth h but also by adding the deflector and increasing its angle. Finally, the overflowrate produced by one wave is not reduced by the 30° deflector, whatever the water depth. On the contrary, the 60° deflector reduces overtopping, which will be further discussed in the following.

	F_{max} [kN m^{-1}]			Imp [kN s m^{-1}]		
h [m]	Vertical wall	Defl. 30°	Defl. 60°	Vertical wall	Defl. 30°	Defl. 60°
13.42	912.05	653.44	500.11	0.058	0.060	0.146
14.42	1627.51	1724.70	5246.07	0.303	0.335	0.449
15.42	12 561.66	17 892.04	25 027.25	0.520	0.792	1.852
	t_{rs} [s]			q_{wave} [m^3]		
h [m]	Vertical wall	Defl. 30°	Defl. 60°	Vertical wall	Defl. 30°	Defl. 60°
13.42	0.160	0.175	0.586	0.103	0.135	0.008
14.42	0.548	0.570	0.444	0.571	0.616	0.462
15.42	0.288	0.285	0.293	1.189	1.195	0.932

Table 2: Maximum force F_{max}, average impulsion Imp, average rising time t_{rs} and overflowrate per wave q_{wave}. Comparison between the three wall geometries for the conditions described in Figure 4.

3.3 Influences of the deflector and the water depth for other wave conditions

The maximum forces applied on the wall (horizontal) and the deflector (vertical and horizontal) are displayed in Figure 7 for four wave conditions and three water depths ($h = 13.42$, 14.42 and 15.42 m). These four wave conditions are characteristics of the 20 conditions and include the most extreme conditions previously discussed: ($T = 8.5$ s, $L = 86.6$ m, $H_S = 1.587$ m), ($T = 9.8$ s, $L = 103.6$ m, $H_S = 4.756$ m), ($T = 8.5$ s, $L = 86.6$ m, $H_S = 3.461$ m), and ($T = 11.1$ s, $L = 120.1$ m, $H_S = 3.57$ m).

Forces get stronger for $\frac{H_S}{L} \sim 0.04$. Moreover, the geometry of the protective wall does not have a significant influence on the forces. As an example, for $h = 15.42$ m and waves conditions fixed to $T = 8.5$ s, $L = 86.6$ m and $H_S = 3.461$ m, the force is 12 561 kN m^{-1} for the vertical wall, 17 892 kN m^{-1} for the wall with a 30° deflector

and 24 094 kN m^{-1} for the wall with a 60° deflector. On the contrary, for h = 15.42 m and waves conditions fixed to T = 11.1 s, L = 120.1 m and H_S = 3.57 m, the force gets 18 745 kN m^{-1}, 14 692 kN m^{-1} and 10 998 kN m^{-1} for the plane wall, the wall with a 30° deflector and the wall with a 60° deflector, respectively. For other cases with breaking impacts, the force reaches its maximum when the wall is equipped with a curved deflector at 30°. Interestingly, forces (and consequently Imp) increase with the wave slope until $H_S/L \simeq 0.04$. After that limit, F and so Imp suddenly decrease. By increasing the wave inclination, waves break against the wall and for $H_S/L \geq 0.04$, waves fall directly on the structure, which reduces drastically the forces and impulsion.

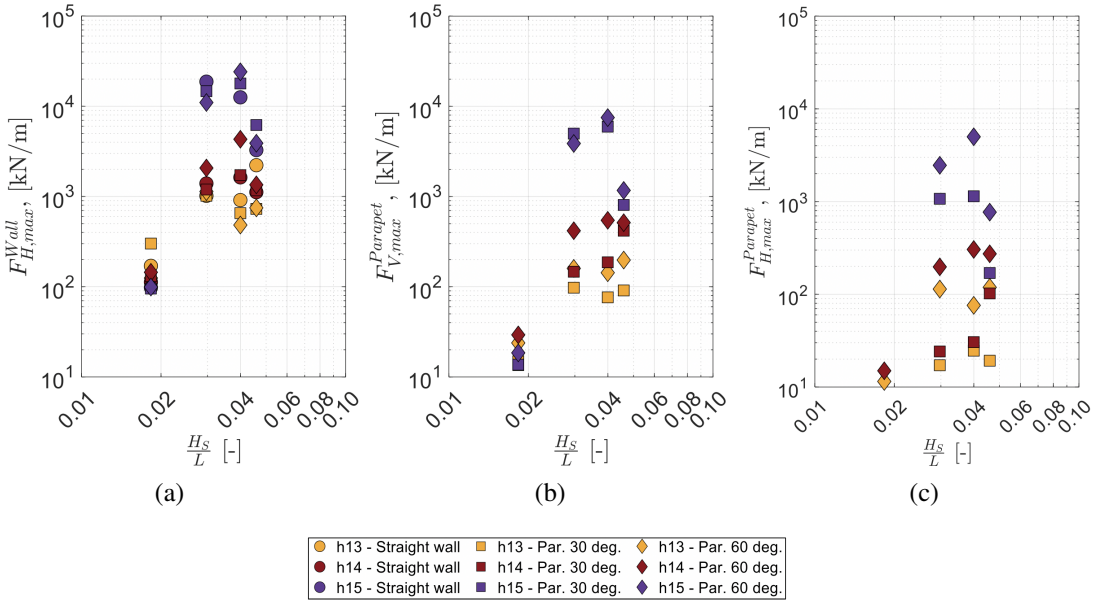

Figure 7: (a) Maximum total force applied on the wall and (b) vertical and (c) horizontal components of the force applied on the deflector as functions of the wave inclination H_S/L. Results obtained for four wave conditions, three water depths and three wall geometries.

For all cases with a deflector, horizontal and vertical forces on the parapet follow the same trend with the same order of magnitude as the total force on the vertical wall. Forces remain always more important for the deflector at 60° compared to the lower angle deflector. This is simply due to the more important direction change imposed to the sprays. The vertical force applied on the deflector represents generally 35% (resp. 30%) of the total (horizontal) force applied on the vertical wall for the 60° (resp. 30°) case. As expected, by increasing the significant wave height H_S, the magnitudes of the forces increase.

The benefit of using a deflector is clearly visible on Figure 8, which represents the ratio k_{bn} between the overtopping flowrates obtained for vertical walls with deflector and without. Whatever the value of the wall relative elevation R_c/H_s, the curved 30° deflector deteriorates the protection against overtopping, especially for breaking waves. It may be explained by the vertical obstruction (0.16 m) offered by this deflector, which remains small compared to the wave amplitude. On the contrary, the 60° deflector, which has a horizontal projection of 0.6 m, drastically improves overtopping. This improvement for the 60° deflector increases from $R_c/H_s \geq 0.5$ to reach up to 95% of overtopping reduction. For $R_c/H_s \leq 0.5$, wave heights are indeed too large compared to the wall. It shows also that the empirical correlation proposed by Kortenhaus et al. [1] fails to predict accurately the right overflowrates. For the 30° deflector, the correlation is not able to predict the deterioration of the performance. For the 60° deflector, the linear decrease of k_{bn} is recovered. The poor performance of this correlation may be partly explained by the fact that their method includes only the horizontal projection of the deflector but not its angle.

4 Conclusions and Future Works

A 2D numerical solver has been extensively used here to investigate the wave impacts on a vertical wall equipped or not with a curved parapet. This solver developed using the OpenFOAM libraries was already carefully validated for two well-documented test cases. Turbulence effects were considered through the $k-\omega$ SST closure, while the Volume of Fluid method enabled to capture the water-air interface. In a former study, it was demonstrated that assuming air as an adiabatic gas is of prime importance for such complex flows, where air pockets may be trapped

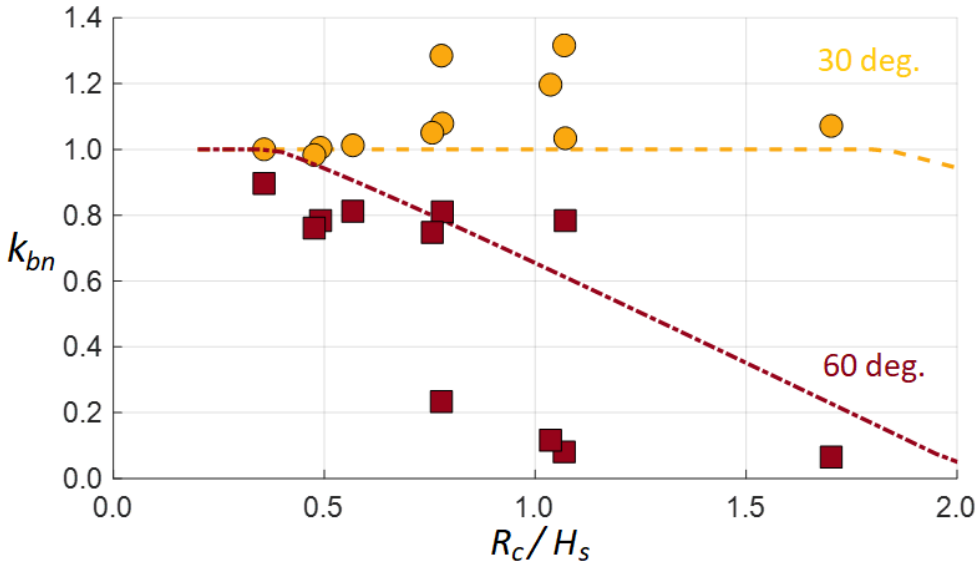

Figure 8: Coefficient of overflowrate variation ($k_{bn} = q_{deflector}/q_{vert-wall}$) as a function of the wall relative elevation (R_c/H_s) - Comparison between the numerical results (symbols) and the correlation of Kortenhaus et *al*. [1] (dashed lines) for two deflector angles (30 and 60°).

during the breaking impacts. The OlaFlow library was coupled to that solver for the wave generation. In total, 20 wave conditions measured by a buoy located in the Gulf of the Saint-Lawrence river (Quebec, Canada) were considered numerically, for three water depths (the base case and two depths mimicking sea-level rise) and three geometries of the protective structure. They corresponded to a plane vertical wall and two vertical walls equipped with a curved parapet with either a 30 or a 60° angle. The main conclusions can be summarized as follows:

- For fixed wave conditions and wall geometry, the maximum force increased with the water depth. Apart from the lower water depth, the presence of the parapet led to an increased maximum force, which also augments with the deflector angle.
- For fixed wave conditions and water depth, the parapet did not significantly affect the rising time of the first impact and consequently, the impulsion varied similarly to the maximum force.
- After a certain wave inclination limit $H_S/L \simeq 0.04$, the maximum force and the impulsion suddenly decreased due to the type of impact.
- The 30° deflector does not reduce overtopping compared to the plane vertical wall and even deteriorates overtopping for most wave conditions and water depths.
- The 60° deflector strongly reduce overtopping by up to 95% compared to the vertical wall, especially for large wall relative elevations.
- The most widely used correlation to predict overtopping failed to predict the right overtopping bahvior.

Future works include the development of a new experimental set-up using the flume available at Université de Sherbrooke to confirm the present results, further validate the numerical model and test a wider range of wave conditions and water depths. From a numerical point of view, it could be interesting to perform some 3D cases to investigate both the influence of the incident wave angle and the sediment transport along the seashore to quantify end-wall effects. The overall long-term objective remains to develop simple correlations and rules to better design protective structures like vertical walls in the context of climate change and sea-level rise.

Acknowledgments

The authors would like to thank the financial support of Ministère des Transports du Québec through the project R828.1. All computations have been performed using the HPC facility provided by the Digital Research Alliance of Canada, which is also gratefully acknowledged.

References

[1] A. Kortenhaus, J. Pearson, T. Bruce, N.W.H. Allsop, and J.W. Van der Meer. Influence of parapets and recurves on wave overtopping and wave loading of complex vertical walls. In *Proc. Coastal Structures*, pages 369–381, Portland (USA), 2003.

[2] A. Kortenhaus, R. Haupt, and H. Oumrraci. Design aspects of vertical walls with steep foreland slopes. In *Proc. Int. Conf. on Breakwaters, Coastal Structures and Coastlines*, pages 220–232, London (UK), 2002. Thomas Telford Publishing.

[3] K.V. Anand, V. Sundar, and S.A. Sannasiraj. Dynamic pressures on curved front seawall models under random waves. *Journal of Hydrodynamics, Ser. B*, 22(5):538–544, 2010.

[4] R.M. Sorensen. *Basic coastal engineering*, volume 10. Springer Science & Business Media, 2005.

[5] W. Allsop, D. Vicinanza, and J.E. McKenna. Wave forces on vertical and composite breakwaters. *Report SR 443, HR Wallingford Ltd, Wallingford, UK*, 1996.

[6] K. McConnell. Derivation, validation and use of parameter map. *MAST III, PROVERBS-Project: Vol. IIa: Hydrodynamic Aspects, Chapter 2.2*, 1999.

[7] G. Cuomo, W. Allsop, T. Bruce, and J. Pearson. Breaking wave loads at vertical seawalls and breakwaters. *Coastal Engineering*, 57(4):424–439, 2010.

[8] M. Castellino, P. Sammarco, A. Romano, L. Martinelli, P. Ruol, L. Franco, and P. De Girolamo. Large impulsive forces on recurved parapets under non-breaking waves. A numerical study. *Coastal Engineering*, 136:1–15, 2018.

[9] G. Sainflou. Essai sur les digues maritimes verticales. *Annales des Ponts et Chaussées*, 98, tome II(4):5–48, 1928.

[10] Y. Goda. New wave pressure formulae for composite breakwaters. *Coastal Engineering Proceedings*, 1(14):1702–1720, 1974.

[11] R.A. Bagnold. Interim report on wave-pressure research. *Excerpt from the J. of the Institution of Civil Engineers*, 1939.

[12] EurOtop II. Manual on wave overtopping of sea defences and related structures. an overtopping manual largely based on european research, but for worldwide application. *European Overtopping Manual*, 2018.

[13] D. Stagonas, R. Ravindar, V. Sriram, and S. Schimmels. Experimental evidence of the influence of recurves on wave loads at vertical seawalls. *Water*, 12:889, 2020.

[14] S. Croquer, S. Poncet, R.W.J. Lacey, and I. Nistor. Statistical analysis and prediction of force and overtopping rates on large-scale vertical walls using support vector machine and random forest regression. *Canadian Journal of Civil Engineering*, 50(5):375–386, 2023.

[15] J. González-Cao, C. Altomare, A.J.C. Crespo, J.M. Domínguez, M. Gómez-Gesteira, and D. Kisacik. On the accuracy of DualSPHysics to assess violent collisions with coastal structures. *Computers & Fluids*, 179:604–612, 2019.

[16] S. Croquer, P. Diaz-Carrasco, V. Tamimi, S. Poncet, R.W.J. Lacey, and I. Nistor. Modelling wave-structure interactions including air compressibility: a case study of breaking wave impacts on a vertical wall along the Saint-Lawrence Bay. *Ocean Engineering*, 273:113971, 2023.

[17] M. Castellino. Confined-crest impact: the influence of the toe berm on the impulsive forces. *Journal of Waterway, Port, Coastal, and Ocean Engineering*, 04024008:1–12, 2024.

[18] Service météorologique du Canada, 2021. https://www.meds-sdmm.dfo-mpo.gc.ca/isdm-gdsi/waves-vagues/index-fra.html. Visité le 01-05-2021.

[19] H. Bredmose, G.N. Bullock, and A.J. Hogg. Violent breaking wave impacts. Part 3. Effects of scale and aeration. *Journal of Fluid Mechanics*, 765:82–113, 2015.

[20] F.R. Menter. Two-equation eddy-viscosity turbulence models for engineering applications. *AIAA Journal*, 32(8):1598–1605, 1994.

[21] I. Gatin, S. Liu, V. Vukčević, and H. Jasak. Finite volume method for general compressible naval hydrodynamics. *Ocean Engineering*, 196:106773, 2020.

[22] B. Devolder, P. Rauwoens, and P. Troch. Application of a buoyancy-modified k-ω SST turbulence model to simulate wave run-up around a monopile subjected to regular waves using OpenFOAM®. *Coastal Engineering*, 125:81–94, 2017.

[23] H. Rusche. *Computational fluid dynamics of dispersed two-phase flows at high phase fractions*. PhD thesis, University of London, 2002.

[24] B.E. Larsen, D.R. Fuhrman, and J. Roenby. Performance of InterFoam on the simulation of progressive waves. *Coastal Engineering Journal*, 61(3):380–400, 2019.

[25] P. Higuera. olaFlow: CFD for waves (v1.1). Software. http://dx.doi.org/10.5281/zenodo.1297013.

[26] P. Higuera, J.L. Lara, and I.J. Losada. Simulating coastal engineering processes with OpenFOAM®. *Coastal*

Engineering, 71:119–134, 2013.

[27] S. Croquer, P. Diaz-Carrasco, V. Tamimi, S. Poncet, J. Lacey, and I. Nistor. Modelling wave-structure interactions including air compressibility: A case study of breaking wave impacts on a vertical wall along the Saint-Lawrence Bay. *Ocean Engineering*, 273:113971, 2023.

[28] M. Darwish and F. Moukalled. *The finite volume method in computational fluid dynamics: an advanced introduction with OpenFOAM® and Matlab®*. Springer, 2016.

[29] C. Loken, D. Gruner, L. Groer, R. Peltier, N. Bunn, M. Craig, T. Henriques, J. Dempsey, C.-H. Yu, J. Chen, et al. SciNet: lessons learned from building a power-efficient top-20 system and data centre. In *Journal of Physics: Conference Series*, volume 256, page 012026. IOP Publishing, 2010.

[30] G.N. Bullock, C. Obhrai, D. Peregrine, and H. Bredmose. Violent breaking wave impacts. Part 1 : Results from large-scale regular wave tests on vertical and sloping walls. *Coastal Engineering*, 54(8):602–617, 2007.

[31] X. Chen, B. Hofland, W. Molenaar, A. Capel, and M.R. Van Gent. Use of impulses to determine the reaction force of a hydraulic structure with an overhang due to wave impact. *Coastal Engineering*, 147:75–88, 2019.